Scripta Materialia 163 (2019) 24–28

Contents lists available at ScienceDirect

Scripta Materialia

journal homepage: www.elsevier.com/locate/scriptamat

Nano-graining a particle-strengthened high-entropy alloy

Dong-Hyun Lee [a], Jeong-Min Park [b], Guanghui Yang [b], Junyang He [a], Zhaoping Lu [c], Jin-Yoo Suh [d], Megumi Kawasaki [e,*], Upadrasta Ramamurty [f,*], Jae-il Jang [b,*]

[a] Department for Microstructure Physics and Alloy Design, Max-Planck-Institut für Eisenforschung GmbH, Düsseldorf 40237, Germany
[b] Division of Materials Science and Engineering, Hanyang University, Seoul 133-791, South Korea
[c] State Key Laboratory for Advance Metals and Materials, University of Science and Technology Beijing, Beijing 10083, People's Republic of China
[d] High Temperature Energy Materials Research Center, Korea Institute of Science and Technology, Seoul 136-791, Republic of Korea
[e] School of Mechanical, Industrial & Manufacturing Engineering, Oregon State University, Corvallis, OR 97331-6001, USA
[f] School of Mechanical & Aerospace Engineering, Nanyang Technological University, Singapore 639798

ARTICLE INFO

Article history:
Received 21 December 2018
Accepted 27 December 2018
Available online xxxx

Keywords:
High-entropy alloy
Particle strengthening
Grain boundary strengthening
High-pressure torsion
Nanoindentation

ABSTRACT

The possibility of further enhancing the strength of a $(CoCrFeNi)_{94}Ti_2Al_4$ high-entropy alloy (HEA), which is already strengthened by $Ni_3(Ti,Al)$ second-phase particles, by grain refinement through high-pressure torsion (HPT) is examined. Concomitant with nanograin formation, HPT was found to induce particle dissolution and structural transformation of the remnant particles. Nanoindentation experiments of nanocrystalline HEA, with and without particles in the pre-HPT microstructure, suggests that grain boundary strengthening is the dominant strengthening mechanism.

High-entropy alloys (HEAs) are of significant current research interest due to their unique single or two phases microstructures and interesting sets of mechanical properties [1–6]. HEAs with the face-centered cubic (fcc) single phase microstructure are often not strong enough for practical structural applications. For example, the most widely studied HEA, CoCrFeMnNi [7,8], has a relatively low yield strength of ~200 MPa at ambient temperature. Therefore, efforts are directed towards enhancing the strength via the exploitation of various mechanisms such as grain boundary (GB) strengthening [9,10] and interstitial solid solution strengthening [11,12], among others. In the grain refinement method of fcc HEAs, the Hall-Petch (HP) strengthening coefficient, which is the slope of the strength vs. $1/\sqrt{d}$ plot where d is the grain size, was found to be significantly higher than that of conventional fcc metals, and was attributed to the enhanced lattice friction [9,10,13,14] for dislocation motion in HEAs due to high concentrations of the solutes and a severely distorted lattice. Thus, reducing d to below ~100 nm, i.e., nanocrystalline (nc) regime, is a viable option for strengthening fcc HEAs [15–17]. Indeed, it was demonstrated that severe plastic deformation (SPD) via high-pressure torsion (HPT) process [18,19] can markedly enhance their strength [20–25].

The possibility of synergizing the above with an additional strengthening mechanism, namely particle or second phase strengthening, is examined in this study. Recently, He et al. [26] reported that the tensile strength of FeCoNiCr HEA doubles–while remaining ductile–upon the introduction of $L1_2$- structured $Ni_3(Al,Ti)$ phase (with the size range of 20–100 nm) that is coherent with the fcc matrix. However, SPD processes can cause the dissolution of the second phase particles, which is widely reported for a number of metallic systems [27–29]. If HEAs are also be susceptible for such dissolution during, and if yes, the trade-offs between the two strengthening mechanisms is investigated in this study.

The $(CoCrFeNi)_{94}Ti_2Al_4$ (at.%) HEA was prepared by arc-melting a mixture of pure metals (purity >99.9%), re-melting at least four times, and then drop-casting into a copper mold. The ingots were subsequently tube-sealed and homogenized at 1473 K for 4 h. The homogenized alloy was first cold rolled (~30% reduction in thickness) and then annealed at 1273 K for 2 h followed by 18 h at 1073 K before water quenching. For comparison, we also examined a homogenized sample without any second-phase particles. Hereafter, the HEA with and without the second-phase particles are referred to as two phase (TP) and single phase (SP) alloys, respectively. Both types of HEA were machined into disks having a radius of 5 mm and a thickness of 0.83 mm. The discs were subjected to HPT processing at room temperature for 1/4, 1/2, 1, and 2 turns (N) under a pressure of 6 GPa.

The microstructures were examined by scanning electron microscopy (SEM; Nova NanoSEM 450, FEI Co., Hillsboro, OR) and TEM (Talos F200X, FEI Co., Hillsboro, OR). During the latter, element mapping using energy dispersive X-ray spectroscopy (EDS) was performed. In

* Corresponding authors.
E-mail addresses: megumi.kawasaki@oregonstate.edu (M. Kawasaki), URAM@ntu.edu.sg (U. Ramamurty), jijang@hanyang.ac.kr (J. Jang).

https://doi.org/10.1016/j.scriptamat.2018.12.033
1359-6462/

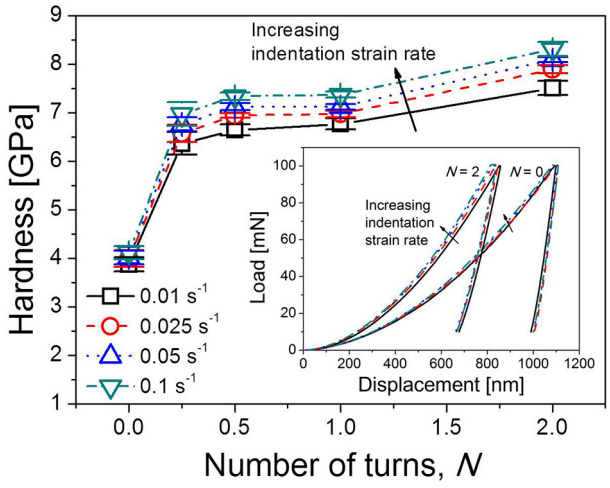

Fig. 1. Changes in nanoindentation hardness value with number of turns and indentation strain rates. Inset shows representative *P*–*h* curves obtained at different rates (for $N = 0$ and 2).

order to obtain TEM samples, focused ion beam (FIB; Nova 200 NanoLab, FEI Co, Hillsboro, OR) milling was performed.

For the nanoindentation experiments, surfaces were mechanically polished and then vibration-polished (VibroMet 2, Buehler, Lake Bluff, IL) with 0.02 μm colloidal silica for 10 h. Nanoindentation tests were conducted at the edge regions of the HPT disks using a Nanoindenter-XP (formerly MTS; now KLA-Tencor, Milpitas, CA) with a Berkovich indenter. The specimens were loaded to $P_{max} = 100$ mN at constant indentation strain rates $\dot{\varepsilon}_i (= h^{-1}(dh/dt) = 0.5P^{-1}(dP/dt)$ [30]) of 0.01, 0.025, 0.05 and 0.1 s^{-1}.

Representative nanoindentation load-displacement (*P*-*h*) curves (for the extreme cases of $N = 0$ and 2) are displayed in the inset of Fig. 1. From the curves, the nanoindentation hardness, *H*, values of the disk edges were estimated according to the Oliver-Pharr method [31]. The variations in *H* as a function of *N* at four different $\dot{\varepsilon}_i$ are plotted in Fig. 1. Two important features in Fig. 1 are noteworthy. First, it is apparent that *H* of all HPT processed disks are much higher than that of alloys before HPT ($N = 0$). This alloy experiences a high rate of hardening in the early stages of HPT; the rate of increase tapers off at higher *N*. Second, as expected from the *P*-*h* curves in the inset, the estimated *H* for each HEA specimen is rate-sensitive and increases with $\dot{\varepsilon}_i$.

Representative results of the microstructural characterization of the TP alloys for ($N = 0$, 1/4, and 2) are summarized in Fig. 2. For each alloy, in addition to the main SEM or TEM images used for grain size evaluation, scanning transmission electron microscopy (STEM) images, elemental maps for "Fe, Co, Cr" and "Ni, Al, Ti" (from EDS mapping), and the selected area electron diffraction (SAED) pattern (of the same area on which STEM was performed) are also displayed. Fig. 2a shows the typical microstructure of the TP alloy before HPT (i.e., $N = 0$), exhibiting that it is coarse-grained in nature with an average *d* of ~57 μm and has a significant amount of fine second-phase particles. In the SAED pattern, the bright spots are from the fcc matrix, and the additional weak spots correspond to the second-phase with the superlattice $L1_2$ structure. They reveal particles, whose size is in tens of nm, enriched with "Ni, Al, Ti" embedded in a compositionally homogeneous matrix. Table 1 lists the average chemical compositions of both the particles and matrix; these were obtained via EDS on more than three different locations. The composition of the particles is similar to that reported previously by He et al. [26]. From these results, we conclude that the $L1_2$ phases is a Ni_3 (Ti, Al) type γ′ phase.

Representative microstructures, obtained from the edge regions of the HPT disks through TEM, are displayed in Fig. 2b and c for $N = 1/4$ and 2, respectively. These bright-field (BF) images reveal that *d* reduced to ~62 and ~24 nm for $N = 1/4$ and 2, respectively. SAED data for both samples exhibit ring patterns indicating to significant grain refinement during HPT without any perceptible texture. On the basis of these observations, we conclude that a nano-grain structure readily develops during HPT, even as early as $N = 1/4$; *d* decreases further–but more gradually–with increasing *N*. In the EDS maps and the STEM images for $N = 1/4$ and 2, while the "Ni, Al, Ti" enriched particles observed in the alloy before HPT ($N = 0$) can still be seen even after HPT, both their size and volume fraction decrease with *N* (see Table 2). This observation suggests that SPD, which the alloy is subjected to via HPT, leads to the gradual dissolution of second-phase particles, which is similar to that reported in other metallic systems [27–29]. A substantial increase in the matrix-particle interface energy due to the dislocation

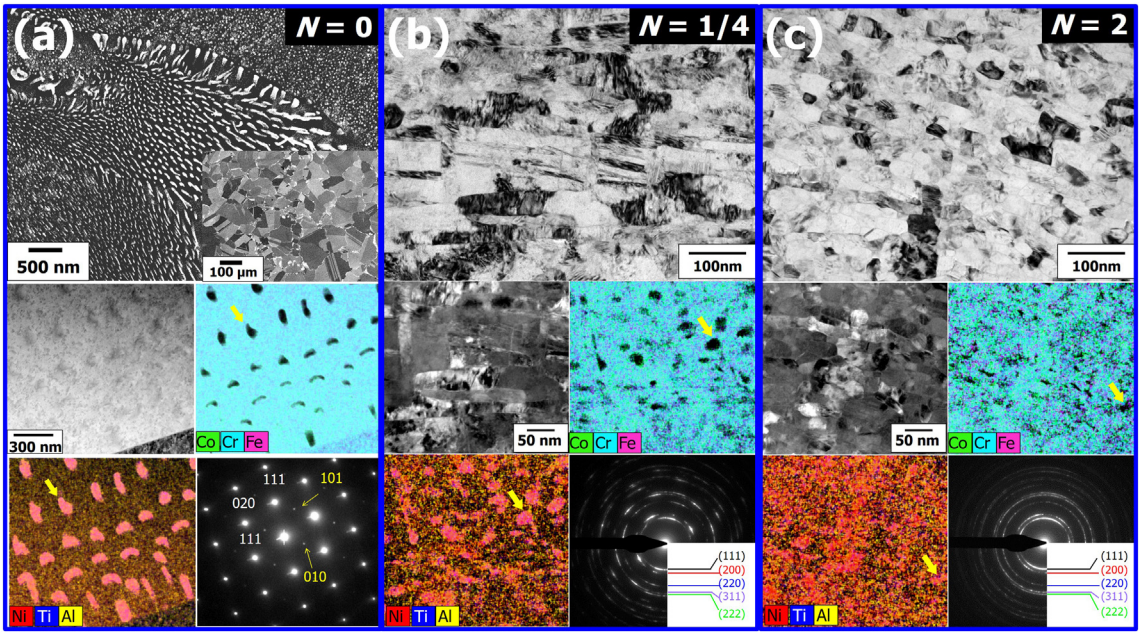

Fig. 2. Typical microstructure of TP alloys (a) before HPT ($N = 0$), and (b) after 1/4 and (c) 2 turns. In addition to SEM or TEM image, each set includes STEM image, elemental distribution map, and SAED pattern.

Table 1
Chemical compositions (at.%) of the phases in TP alloy.

Phase	Process	Co [at.%]	Cr [at.%]	Fe [at.%]	Ni [at.%]	Al [at.%]	Ti [at.%]
Matrix	AR	25.3 ± 0.2	22.5 ± 0.2	24.8 ± 0.1	24.9 ± 0.1	1.9 ± 0.1	0.8 ± 0.1
	$N = 1/4$	25.3 ± 0.6	23.0 ± 0.2	25.3 ± 0.2	23.1 ± 1.1	2.6 ± 0.1	0.7 ± 0.1
	$N = 2$	23.0 ± 1.4	21.3 ± 1.5	23.9 ± 1.1	26.4 ± 3.9	2.9 ± 0.1	1.6 ± 0.1
NiAlTi-rich phase	AR	11.7 ± 0.4	1.8 ± 0.4	4.4 ± 0.6	66.3 ± 1.3	6.0 ± 0.2	9.8 ± 0.1
	$N = 1/4$	16.3 ± 0.1	6.9 ± 0.5	10.6 ± 1.2	50.7 ± 2.1	7.2 ± 0.8	8.4 ± 0.3
	$N = 2$	16.9 ± 0.8	10.0 ± 0.7	12.3 ± 2.5	47.1 ± 1.8	7.7 ± 0.7	6.0 ± 1.6

accumulation during plastic deformation was suggested as the main driving force for this phenomenon. It appears, however, that the dissolution is incomplete, as some particles could still be seen in the HPT-processed TP alloys (Fig. 2). Interestingly, the near-complete disappearance of the superlattice reflections corresponding to $L1_2$ structure in the SAED pattern suggests that the structure of remnant particles changes from ordered $L1_2$ to disordered fcc.

The above results suggest that the marked increase in H of TP HEA upon HPT is mainly due to grain refinement. To assess the contribution of the remnant particles on H of nc TP alloy, if any, we performed HPT on SP samples (having the same composition, but without particles) and probed them via nanoindentation and TEM (see Figs. S1 and S2 of Supplementary Material). Microstructural analysis (Fig. S2) reveals that HPT leads to a substantial grain refinement in this case too (d ~ 71 and ~39 nm for $N = 1/4$ and 2, respectively). A homogeneous distribution of constituent elements without any obvious segregation or clustering is maintained as well.

The empirical relation that relates H to the flow stress s, suggested by Tabor [32]: $H = C\sigma$ where C is the constraint factor (often = 3) is utilized to convert the HP relation in terms H as $H = H_0 + k_{HP}{}^{-1/2}$ where H_0 is the 'intrinsic hardness' and k_{HP} is the HP coefficient (or locking parameter). Fig. 3 shows the variation of H as a function of $d^{-0.5}$ for both the examined alloys. A good linear fit between H and $d^{-20.5}$ following the HP relation is noted for the SP alloy (black solid line) with a k_{HP} of ~28.6 MPa·mm$^{1/2}$. This k_{HP} is in good agreement with that reported for other single fcc phase HEA (~27.7 MPa·mm$^{1/2}$ [21]), leading us to conclude that the significant hardening of SP alloy by HPT is mainly due to grain refinement (and not work hardening).

According to a previous study [26], the yield strength (YS) increment that accrues due to second-phase particles, $\Delta\sigma_p$, in TP alloy is ~326.7 MPa, which translates to ~980 MPa in terms of H as per the Tabor's relation [33]. The latter is close to the difference of ~1100 MPa in H of TP and SP alloys (at $N = 0$), confirming that the higher H of the TP alloy is indeed due to particle strengthening. If this were to occur simultaneously with strengthening associated with the grain size reduction in the HPT processed TP alloys, the variation in its H with d should follow the dashed red line in Fig. 3, which was drawn assuming that the contributions of the two mechanisms to strength of HEA can be linearly superposed according to the relation: $H = H_0 + k_{HP}d^{-1/2} + \Delta H_p$ (where ΔH_p is the H increment due to the particles). However, the experimental H values of the HPT processed TP alloys are significantly lower; in fact they appear to follow the black HP line drawn for the SP alloy. This observation implies that the hardening in the HPT processed HEA arises mainly as a consequence of substantial grain refinement. It further implies that the second phase particles cease to contribute to the strength of the TP alloy once it undergoes HPT. (For $N = 2$, one may note that H of TP HEA is higher than that of SP HEA, which is possibly due to the difference in d (~24 and ~39 nm for TP and SP alloys, respectively). Accelerated grain refinement in TP alloys could be aided by the development of local deformation zones, which contain high dislocation density, around the second-phase particles during deformation, [34–37].)

The above result clearly demonstrates that the remnant particles' contribution to strength is insignificant. Since their structure changes from ordered $L1_2$ to disordered fcc, it is conceivable that the resistance offered by these transformed particles is similar to that of the matrix (recall that the matrix is itself highly solid solution strengthened). Hence, they may It is worth noting that HPT has indeed been reported to cause a polycrystalline Ni_3Al intermetallic alloy with $L1_2$ structure to a disordered nc structure [38–41]. The destruction of the ordered structure during HPT can take place by different mechanisms such as antiphase boundary (APB) tube formation, dislocation glide and annihilation [40–42].

To understand the thermally activated plastic deformation mechanisms in the HEAs under examination, we evaluated the strain-rate sensitivity (SRS), m, and activation volume, V^* [43–45] using the equations $m = (\partial \ln(H/C)/\partial \ln\dot{\varepsilon}_i)_{\varepsilon,T}$ and $V^* = \sqrt{3}k_BT(\partial \ln\dot{\varepsilon}_i/\partial(H/C))_{\dot{\varepsilon},T}$ where k_B is Boltzmann constant and T is the absolute temperature. Representative double-logarithmic plots of H/C versus $\dot{\varepsilon}_i$ and logarithmic $\dot{\varepsilon}_i$ versus linear H/C are displayed in the insets of Fig. 4 (for TP alloy). The values of m and V^* extracted from such plots are plotted as a function of N for both TP and SP alloys in Figs. 4a and b, respectively. The magnitude of the Burgers vector, b, used for computing V^* was taken as ~0.253 nm [26]. At $N = 0$, the values of m (~0.027 and ~0.024) are similar for both TP and SP alloys, and the corresponding V^* are ~17b^3 and ~13b^3. They are also similar to those reported for coarse-grained single fcc phase HEAs [21,46–48]. In those alloys, plastic deformation is governed by the features that are intrinsic to HEA such as severely distorted lattice rather

Table 2
Size and volume fractions of second-phase particles in TP alloy.

Condition	Particle size [nm]	Volume fraction [%]
AR	<40 [26]	~23.3 [26]
$N = 1/4$	~20.4	~25.2
$N = 2$	~12.8	~14.2

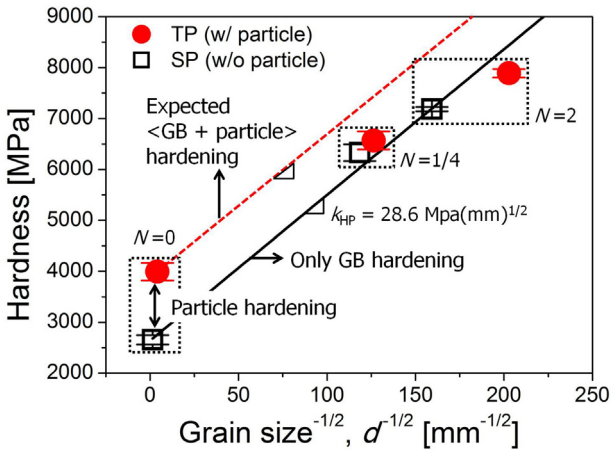

Fig. 3. Changes in hardness H as a function of grain size d in TP and SP alloy. Hall-Petch plot and its slope k_{HP} are for SP alloy.

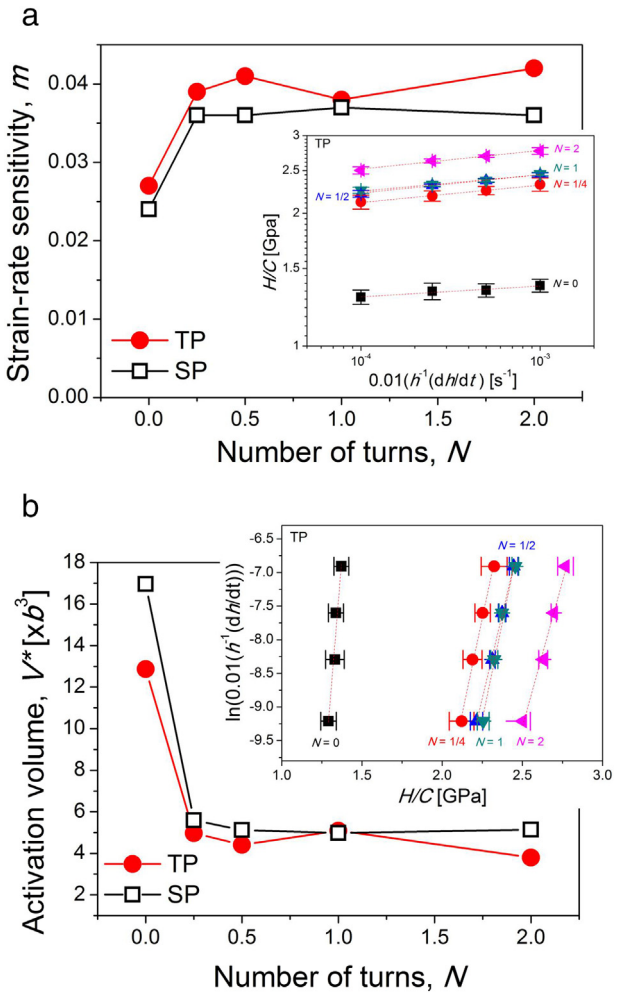

Fig. 4. Variations in (a) strain-rate sensitivity and (b) activation volume with increasing *N*. Insets show the relations between stress and strain rate for TP alloy.

than by dislocation forest cutting that is typical in conventional metals and alloys.

After HPT for $N = 1/4$, m of TP alloy increases significantly to ~0.039; thereafter it remains nearly-invariant. Since a higher m generally indicates to a larger capacity for plastic deformation, we infer that the fine-grained HEA, obtained via HPT, would not only be strong but also be able to accommodate plasticity, as compared to its coarse grained counterpart. Note that the presence of second phase particles in an alloy does not typically affect the thermally activated dislocation processes [49], i.e., both m and V^* are unlikely to be affected whether the alloy is second phase strengthened or not. For this reason, the trends observed in both these properties, observed in Fig. 4, are similar.

It is well known for conventional fcc metals and alloys, nanocrystallisation leads to a two orders of magnitude reduction in V^* for dislocation-mediated flow; from ~1000 b^3 to ~10 b^3 [45,50]. Such a massive reduction is due to the onset of the critical roles that GBs play in the plastic deformation by both interacting with and as sources of dislocations [43,45]. Thus, a marked reduction V^* upon HPT in both the HEAs under investigation (see Fig. 4b), is expected. Since V^* in the nano-grained HEA, whether it contains secondary phases or not, is well below ~10b^3, it appears that the deformation mechanism is similar to conventional nc metals as in GB-mediated dislocation activity [17,44]. On this basis, we surmise that the predominant deformation mechanism changes from the distorted lattice controlled one to that of a GB-mediated one.

Finally, a comparison of some of the properties of the HEA measured in this study with those of conventional nc metals might be instructive. As already mentioned, k_{HP} of the present HEA (~28 MPa·mm$^{1/2}$) is significantly higher (by ~55%) than even the upper bound value of k_{HP} reported for Ni, which was also probed into the nc regime. Note that Hughes et al. [51] indicate that k_{HP} for Ni lies within the range of 3.9 to 18 MPa·mm$^{1/2}$. If one was to take the mean value of this range, k_{HP} of HEA would be ~150% higher. Since k_{HP} is an indicator of the resistance offered by the lattice to dislocation glide, a large value of it indicates the high lattice friction offered by HEA [9,10,13,14]. With regard to m, while m of nc HEA, measured in the present study, fall within the range reported for nc Ni (see the literature summary in [52,53]), direct comparisons and broad conclusions on that basis are difficult due to the fact that the range of m reported for nc Ni is very large, and varies considerably with the testing method, applied range of strain rate, and applied stress [52,53].

The work at Hanyang University was supported by the National Research Foundation of Korea (NRF) grants funded by the Ministry of Science and ICT (No. 2015R1A5A1037627 and No. 2017R1A2B4012255). The work at Oregon State University was supported by the National Science Foundation of the United States under Grant No. DMR-1810343.

Appendix A. Supplementary data

Supplementary data to this article can be found online at https://doi.org/10.1016/j.scriptamat.2018.12.033.

References

[1] Y. Zhang, T.T. Zuo, Z. Tang, M.C. Gao, K.A. Dahmen, P.K. Liaw, Z.P. Lu, Prog. Mater. Sci. 61 (2014) 1–93.
[2] B. Gludovatz, A. Hohenwarter, D. Catoor, E.H. Chang, E.P. George, R.O. Ritchie, Science 345 (2014) 1153–1158.
[3] C.C. Tasan, Y. Deng, K.G. Pradeep, M.J. Yao, H. Springer, D. Raabe, JOM 66 (2014) 1993–2001.
[4] D.B. Miracle, O.N. Senkov, Acta Mater. 122 (2017) 448–511.
[5] Z. Wu, M.C. Troparevsky, Y.F. Gao, J.R. Morris, G.M. Stocks, H. Bei, Curr. Opin. Solid State Mater. Sci. 21 (2017) 267–284.
[6] Y. Zhao, D.-H. Lee, M.-Y. Seok, J.-A. Lee, M.P. Phaniraj, J.-Y. Suh, H.-Y. Ha, J.-Y. Kim, U. Ramamurty, J.-i. Jang, Scr. Mater. 135 (2017) 54–58.
[7] B. Cantor, I.T.H. Chang, P. Knight, A.J.B. Vincent, Mater. Sci. Eng. A 375 (2004) 213–218.
[8] B. Cantor, Entropy 16 (2014) 4749–4768.
[9] W.H. Liu, Y. Wu, J.Y. He, T.G. Nieh, Z.P. Lu, Scr. Mater. 68 (2013) 526–529.
[10] F. Otto, A. Dlouhý, C. Somsen, H. Bei, G. Eggeler, E.P. George, Acta Mater. 61 (2013) 5743–5755.
[11] Z. Li, C.C. Tasan, H. Springer, B. Gault, D. Raabe, Sci. Rep. 7 (2017) 40704.
[12] M. Wang, Z. Li, D. Raabe, Acta Mater. 147 (2018) 236–246.
[13] Y.L. Zhao, T. Yang, Y. Tong, J. Wang, J.H. Luan, Z.B. Jiao, D. Chen, Y. Yang, A. Hu, C.T. Liu, J.-J. Kai, Acta Mater. 138 (2017) 72–82.
[14] S. Yoshida, T. Bhattacharjee, Y. Bai, N. Tsuji, Scr. Mater. 134 (2017) 33–36.
[15] H. Gleiter, Prog. Mater. Sci. 33 (1989) 223–315.
[16] M.A. Meyer, A. Mishra, D.J. Benson, Prog. Mater. Sci. 51 (2006) 427–556.
[17] M. Dao, L. Lu, R.J. Asaro, J.T.M. De Hosson, E. Ma, Acta Mater. 55 (2007) 4041–4065.
[18] A.P. Zhilyaev, G.V. Nurislamova, B.K. Kim, M.D. Baró, J.A. Szpunar, T.G. Langdon, Acta Mater. 51 (2003) 753–765.
[19] A.P. Zhilyaev, T.G. Langdon, Prog. Mater. Sci. 53 (2008) 893–979.
[20] B. Schuh, F.M. Martin, B. Völker, E.P. George, H. Clemens, R. Pippan, A. Hohenwarter, Acta Mater. 96 (2015) 258–268.
[21] D.-H. Lee, I.-C. Choi, M.-Y. Seok, J. He, Z. Lu, J.-Y. Suh, M. Kawasaki, T.G. Langdon, J.-i. Jang, J. Mater. Res. 30 (2015) 2804–2815.
[22] D.-H. Lee, M.-Y. Seok, Y. Zhao, I.-C. Choi, J. He, Z. Lu, J.-Y. Suh, U. Ramamurty, M. Kawasaki, T.G. Langdon, J.-i. Jang, Acta Mater. 109 (2016) 314–322.
[23] C.C. Koch, J. Mater. Res. 32 (2017) 3435–3444.
[24] B. Schuh, B. Völker, J. Todt, N. Schell, L. Perrière, J. Li, J.P. Couzinié, A. Hohenwarter, Acta Mater. 142 (2018) 201–212.
[25] N.D. Stepanov, N.Yu. Yurchenko, A.O. Gridneva, S.V. Zherebtsov, Yu.V. Ivanisenko, G.A. Salishchev, Mater. Sci. Eng. A 716 (2018) 308–315.
[26] J.Y. He, H. Wang, H.L. Huang, X.D. Xu, M.W. Chen, Y. Wu, X.J. Liu, T.G. Nieh, K. An, Z.P. Lu, Acta Mater. 102 (2016) 187–196.
[27] J. Languillaume, G. Kapelski, B. Baudelet, Acta Mater. 45 (1997) 1201–1212.
[28] Z. Liu, S. Bai, X. Zhou, Y. Gu, Mater. Sci. Eng. A 528 (2011) 2217–2222.
[29] D.-H. Lee, J.-A. Lee, Y. Zhao, Z. Lu, J.-Y. Suh, J.-Y. Kim, U. Ramamurty, M. Kawasaki, T.G. Langdon, J.-i. Jang, Acta Mater. 140 (2017) 443–451.
[30] B.N. Lucas, W.C. Oliver, Metall. Mater. Trans. A 30A (1999) 601–610.
[31] W.C. Oliver, G.M. Pharr, J. Mater. Res. 7 (1992) 1564–1583.
[32] D. Tabor, Hardness of Metals, Oxford University Press, UK, 1951.

[33] S. Shim, J.-I. Jang, G.M. Pharr, Acta Mater. 56 (2008) 3824–3832.
[34] F.J. Humphreys, Acta Metall. 27 (1979) 1801–1814.
[35] F.J. Humphreys, M. Hatherly, Recrystallization and Related Annealing Phenomena, Pergamon, UK, 1995.
[36] P.J. Apps, J.R. Bowen, P.B. Prangnell, Acta Mater. 51 (2003) 2811–2822.
[37] I. Gutierrez-Urrutia, M.A. Muñoz-Morris, D.G. Morris, Mater. Sci. Eng. A 394 (2005) 399–410.
[38] R.Z. Valiev, A.K. Mukherjee, Scr. Mater. 44 (2001) 1747–1750.
[39] A.V. Korznikov, G. Tram, O. Dimitrov, G.F. Korznikova, S.R. Idrisova, Z. Pakiela, Acta Mater. 49 (2001) 663–671.
[40] C. Rentenberger, H.P. Karnthaler, Acta Mater. 53 (2005) 3031–3040.
[41] C. Rentenberger, H.P. Karnthaler, Acta Mater. 56 (2008) 2526–2530.
[42] C. Rentenberger, T. Waitz, H.P. Karnthaler, Phys. Rev. B 67 (2003) 094109.
[43] E. Ma, Science 305 (2004) 623–624.
[44] R.J. Asaro, S. Suresh, Acta Mater. 53 (2005) 3369–3382.
[45] Y.M. Wang, A.V. Hamza, E. Ma, Acta Mater. 54 (2006) 2715–2726.
[46] Z. Wu, Y. Gao, H. Bei, Acta Mater. 120 (2016) 108–119.
[47] V. Maier-Kiener, B. Schuh, E.P. George, H. Clemens, A. Hohenwarter, J. Mater. Res. 32 (2017) 2658–2667.
[48] D.-H. Lee, I.-C. Choi, G. Yang, Z. Lu, M. Kawasaki, U. Ramamurty, R. Schwaiger, J.-i. Jang, Scr. Mater. 156 (2018) 129–133.
[49] S. Zhang, W. Hu, R. Berghammer, G. Gottstein, Acta Mater. 58 (2010) 6695–6705.
[50] F.D. Torre, P. Spätig, R. Schäublin, M. Victoria, Acta Mater. 53 (2005) 2337–2349.
[51] G.D. Hughes, S.D. Smith, C.S. Pande, H.R. Johnson, R.W. Armstrong, Scr. Metall. 20 (1986) 93–97.
[52] I.-C. Choi, B.-G. Yoo, Y.-J. Kim, M.-Y. Seok, Y.M. Wang, J.-i. Jang, Scr. Mater. 65 (2011) 300–303.
[53] I.-C. Choi, Y.-J. Kim, M.-Y. Seok, B.-G. Yoo, J.-Y. Kim, Y.M. Wang, J.-i. Jang, Int. J. Plast. 41 (2013) 53–64.